Soft Matter

SAXS-guided unbiased coarse-grained Monte Carlo simulation for identification of self-assembly nanostructure and dimension

Journal:	*Soft Matter*
Manuscript ID	SM-ART-05-2022-000601.R1
Article Type:	Paper
Date Submitted by the Author:	15-Jun-2022
Complete List of Authors:	Pahari, Silabrata; Texas A&M University System Liu, Shuhao; Texas A&M University College Station, Chemical Engineering Lee, Chi Ho; Texas A&M University System Akbulut, Mustafa; Texas A&M University, Chemical Engineering; Kwon, Joseph; Texas A&M University System,

Soft Matter

ARTICLE TYPE

Cite this: DOI: 00.0000/xxxxxxxxxx

SAXS-guided unbiased coarse-grained Monte Carlo simulation for identification of self-assembly nanostructure and dimension†

Silabrata Pahari,[ab] Shuhao Liu,[a] Chi Ho Lee,[ab] Mustafa Akbulut,[ab] Joseph Sang-Il Kwon *[ab]

Received Date
Accepted Date

DOI: 00.0000/xxxxxxxxxx

Recent studies show that solvated amphiphiles can form nanostructured self-assemblies called dynamic binary complexes (DBCs) in the presence of ions. Since the nanostructures of DBCs are directly related to their viscoelastic properties, it is important to understand how the nanostructures change under different solution conditions. However, it is challenging to obtain a three-dimensional molecular description of these nanostructures by utilizing conventional experimental characterization techniques or thermodynamic models. To this end, we combined the structural data from small angle X-ray scattering (SAXS) experiments and thermodynamic knowledge from coarse-grained Monte Carlo (CGMC) simulations to identify the detailed three-dimensional nanostructure of DBCs. Specifically, unbiased CGMC simulations are performed with SAXS-guided initial conditions, which aids us to sample accurate nanostructures in a computationally efficient fashion. Henceforth, an elliptical bilayer nanostructure is obtained as the most probable nanostructure of DBCs whose dimensions are validated by scanning electron microscope (SEM) images. Then, utilizing the obtained molecular model of DBCs, we could also explain the pH tunability of the system. Overall, our results from SAXS-guided unbiased CGMC simulations highlight that using potential energy combined with SAXS data, we can distinguish otherwise degenerate nanostructures resulting from the inherent ambiguity of SAXS patterns.

1 Introduction

Over the last decade, there has been an increasing interest in industry and academia to develop complex fluids that can change their rheological properties reversibly in response to the changes in solution conditions[1,2]. These reversible fluids find great applications in the pharmaceutical, oil and gas, and speciality chemical industry sectors[3–5]. Specifically, the reversible nature of these fluids is attained via the dynamic nanostructure of self-assembled amphiphiles which are the primary building blocks of these complex fluids. By carrying out further characterization and detailed free energy calculations, it was revealed that these self-assemblies have unique nanostructures. Some of the common nanostructures identified include bilayers, spherical, and wormlike micelles. Identification of these nanostructures is necessary as significant changes in the viscoelastic properties of the materials take place with the varying nanostructure of these materials. For example, the wormlike micelles, which are polymer-like flexible supramolecular self-assemblies, entangle to give higher viscoelasticity than spherical micelles that form no entanglements. Therefore, it has been widely studied to develop novel nanostructures of the supramolecular self-assemblies to attain target rheological properties[6].

Recently, complex self-assembly called dynamic binary complex (DBC) has been synthesized by Liu et al.[7] via the complexation between the zwitterionic beaten type of amphiphiles octadecylamidopropyl (OAPB) and diethylenetriamine (DTA) ions. Specifically, DBCs have a unique viscoelastic property which shows sensitivity to the solution conditions like pH. In recent studies[6,7], it was observed that DBCs consist of tubular nanostructures, and the viscoelastic properties of DBCs are determined by the entanglement process of these tubular nanostructures whose cross-sectional dimensions are almost an order of magnitude larger than those of the conventional tubular wormlike micelles (WLMs). It is difficult to rely on the existing imaging techniques like transmission electron microscopy (TEM) to image microgels such as DBCs. These techniques employ artificial treatments like dehydration, which can often lead to inaccurate imaging results due to significant changes in the morphology of

a Texas A&M University, Artie McFerrin Department of Chemical Engineering, Texas A&M University, College Station, TX 77843, USA.
b Texas A&M Energy Institute, Texas A&M Energy Institute, 1617 Research Pkwy, College Station, TX 77843, USA.
* Corresponsing author, email:kwonx075@tamu.edu

† Electronic Supplementary Information (ESI) available: [details of any supplementary information available should be included here]. See DOI: 10.1039/cXsm00000x/

microgels[8]. Specifically, when DBCs are dehydrated and the entrapped water molecules are removed, strong head-group interactions among the amphiphilic monomers can lead to their aggregation, thus making their accurate characterization difficult in dehydrated phase. To address these limitations, methods like cryogenic transmission electron microscopy (cryo-TEM) can be utilized to obtain high-resolution nanostructure of DBCs in the hydrated phase[9,10]. However, sample preparation is challenging in cryo-TEM[11]; additionally, rapid cooling may perturb the amphiphile conformation, and also the contrast is extremely poor in these methods, leading to low image quality[12]. These challenges have limited the application of cryo-TEM to identify the nanostructures present in microgels like DBCs. Furthermore, when scattering methods like small-angle X-ray scattering techniques (SAXS) are used to obtain the high-resolution three-dimensional nanostructures of DBCs in dispersed phase[13,14], there is an inherent challenge associated with the degeneracy resulting from the reconstruction of three-dimensional nanostructures from a one-dimensional SAXS scattering profile[15–18]. Henceforth, solely utilizing SAXS scattering profiles, only simple structural features such as radius of gyration and maximum diameter of the nanostructures can be extracted[19–22]. However, this knowledge is not sufficient in establishing the structure-property relationships of DBCs[23,24].

Motivated by the challenges associated with analyzing the detailed three-dimensional nanostructures of DBCs, we combine results from experimental characterization techniques and molecular simulations to derive a molecular model of DBCs that can provide us a detailed picture of their nanostructure. Specifically, this molecular model is discovered by considering multiple interactions to understand how the nanostructure of DBCs is affected by varying solution conditions.

In the past, several studies have combined experimental characterization results with molecular simulations by performing SAXS-guided molecular dynamics simulations to sample the native structure of biopolymers[25–28]. Specifically, SAXS data is utilized in these procedures because of its widespread application in structural characterization of both structured and intrinsically disordered molecules in solution. In these methods, a pseudo-energy term is added to the system's hamiltonian based on the discrepancy between the experimentally observed SAXS data and computationally derived profiles. This bias term guides the simulations to reach states that can replicate the experimentally measured SAXS profiles. Although the energy landscapes of these simulations are biased and the total potential energies calculated from these simulations are not accurate, the ability of the methodology to sample conformations of biopolymers that are inaccessible by conventional molecular simulations received much attention[29]. However, it is challenging to directly implement SAXS-guided molecular-scale simulations to sample the detailed nanostructure of DBCs because of the huge computational cost associated with the *ab-initio* calculation of SAXS profiles for large nanostructures like DBCs.

To avoid this computational issue, we explore how unbiased molecular simulations with coarse-grained models can be combined with SAXS to obtain the most probable nanostructures of DBCs. Specifically, using unbiased sampling allows us to avoid the computation of SAXS-biased pseudo-energy term via *ab-initio* Debye's equation, and coarse-graining the molecular models further improves the computational efficiency of the unbiased sampling method. Furthermore, we use the information from SAXS experimental data as the seed selection criterion for coarse-grained Monte Carlo simulations (CGMC)[30–33]. This is achieved by converting the SAXS profile into a discrepancy value which measures dissimilarity between a target SAXS profile (i.e., experimental SAXS profile) and SAXS profiles computed theoretically from molecular models. Subsequently, an iterative search procedure is implemented, where parallel CGMC simulations are seeded with a number of nanostructures with varying dimensions. Unlike the conventional SAXS-guided simulations, in the unbiased sampling procedure implemented in this work, the system's total energy is not modified. Therefore, the total potential energy computed from the SAXS-guided unbiased CGMC simulations is defined as an additional metric to identify the nanostructures of the DBCs. Henceforth, minimizing the total potential energy and SAXS discrepancy values, we could determine the most probable nanostructures of DBCs.

2 Methods

In this section, the different methods implemented to obtain the three-dimensional nanostructure of DBCs are highlighted.

2.1 SAXS-guided seed generation

The idea behind SAXS-guided unbiased sampling is to perform an iterative search where parallel MC simulations are performed, and based on some important structural features, probable nanostructures are identified. Subsequently, new simulations are seeded from these nanostructures. Seeding nanostructures based on SAXS intensity profiles is the primary factor that allows us to bias the search direction while leaving the total potential energy of the system unchanged. Specifically, in the unbiased SAXS-guided MC simulations, the hamiltonian of the system is not modified, which as a result preserves the accuracy of the energy computed from the MC simulations. In this unbiased sampling procedure, iterations are continued until a reasonably accurate nanostructure is identified. The information of the SAXS intensity profile is incorporated in this procedure via the SAXS discrepancy value defined in the following equation:

$$\chi^2 = 1/N \sum_{i=1}^{N} \left[log(I_{cal}(q_i)) - log(I_{exp}(q_i)) \right]^2 \quad (1)$$

where N is the number of data points in the SAXS profile, $I_{cal}(q_i)$ is the calculated SAXS profile, and $I_{exp}(q_i)$ is the experimentally measured SAXS profile. It is to be noted that the lower the SAXS discrepancy value is, the closer the obtained nanostructure is to the true DBC nanostructure. The seeded nanostructures for performing the SAXS-guided MC simulations are obtained from results mentioned in previously published experimental characterization studies[34–36].

In calculating the SAXS discrepancy values, the computationally derived SAXS profiles are obtained from the Debye's equa-

tion. The SAXS scattering intensities are calculated within the range of 0-0.25 $Å^{-1}$. In SAXS calculations, the solvent effect is considered by modeling the solvent as an electron gas with density equal to the average electron density of the solvent, which is equal to 0.334 $e/Å^3$. Furthermore, the hydration shell around the nanostructures is modeled as a double layer with its contrast being equal to 0.03 $e/Å^3$. The details of calculating the *ab-initio* SAXS profiles by considering the effect of solvent and hydration shells are highlighted in Appendix A1.

2.2 MC simulation and coarse-grained force-field

MC simulations are primarily utilized to calculate the total potential energies of seeded nanostructures at equilibrium. The implemented MC simulation consists of simple and segment-wise configurational biased MC (CBMC) moves and a coarse-grained force-field. Specifically, as DBCs consist of long flexible chains like OAPB amphiphiles and DTA ions[7], it is important that an efficient sampling scheme needs to be applied that allows us to explore the dihedral and eulerian angluar domains efficiently. This is done with a segment-wise CBMC simulation scheme where the molecules are regrown in a segmentwise fashion[37]. Further details of implementing the MC simulation is highlighted in Appendix A2 of the supplementary material.

To reduce the computational time and improve the sampling efficiency of the MC simulations, a coarse-graining methodology is implemented. In this methodology, the molecules are not represented by individual atoms, but by beads that approximate a group of atoms. Therefore, utilizing the coarse-grained models in MC simulations significantly reduces the number of interacting centers, thereby the computation time[38].

Subsequently, a coarse-grained force-field is utilized to model the interactions between the coarse-grained molecules in the system. Specifically, the bonded and non-bonded interaction parameters and equations between the coarse-grained molecules are derived from the Martini-3 force-field.[39]. Therefore, the MC simulations performed in this work are primarily coarse-grained Monte Carlo simulations (CGMC). Further details of the force-field considered and the coarse-graining procedure are highlighted in Appendix A3 of the supplimentary information.

2.3 Seeding SAXS-guided nanostructures to unbaised CGMC

The developed SAXS-guided unbiased CGMC sampling procedure begins by considering a set of initial nanostructures. These initial seeds or nanostructures generated for performing SAXS-guided coarse-grained Monte Carlo (CGMC) simulations are derived from the results of various characterization and simulation efforts reported in previous literature studies[40–49]. Specifically, sixty-five geometries are considered for seeding the nanostructures to the developed SAXS-guided sampling scheme. The basis for screening these sixty-five geometries originates from the known information that the characteristic length of DBC is a few hundreds of nanometers. This knowledge about the system helps us significantly narrow down our search by eliminating many of the geometries existing in the literature for general amphiphile self-assemblies. For example, supramolecular self-assemblies like WLMs and globular micelles are eliminated because their characteristic lengths are limited by the size of the amphiphiles (i.e., size of OAPB molecules), which at most extend to values of 6-10 nm. It is to be noted that vesicular structures formed by the folding of bilayers are feasible and probable candidates as they can be of large characteristic dimensions. After we decided to focus on the vesicular structures, all the geometries identified as a result of folding bilayers reported in the literature were considered in this work. For the purpose of demonstration, we have highlighted a few of the geometries considered to generate the initial seeds in Fig. 1. Subsequently, we have considered a set of twenty dimensions of the characteristic lengths for each of these geometries. Therefore, we seed the SAXS-guided coarse-grained sampling procedure with 1300 nanostructures of varying dimensions and geometry.

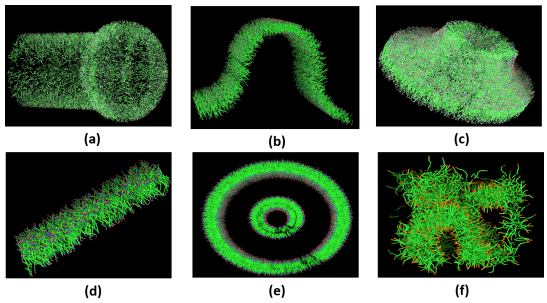

Fig. 1 Demonstration of a few initial seeds considered for SAXS-guided coarse-grained Monte Carlo simulation, (a) sphere-cylindrical structure, (b) buckle structures, (c) torroidal geometry, (d) flat bilayer structure, (e) elongated bilayer cylindrical, and (f) networked tubular structure.

The twenty different nanostructures that are seeded from the initial nanostructures, have values for their characteristic dimensions chosen within the interval from 100 nm to 1000 nm. Specifically, at every iteration the dimensions of the nanostructures are chosen in the interval between $max(0, l_p - dl_{max}/n)$ and $min(1000, l_p + dl_{max}/n)$, where $dl_{max} = 1000$ nm, n is the iteration number, and l_p is the characteristic length of the seeding nanostructure. Once the dimensions of the nanostructures are obtained, parallel CGMC simulations for all the seeded nanostructures are launched, and their total potential energy at equilibrium is evaluated. Then, nanostructures having lowest total potential energies and SAXS discrepancy values are selected for the subsequent iterations. The developed SAXS-guided unbiased CGMC sampling procedure continues until improvement in SAXS discrepancy values and total potential energy values becomes insignificant.

Remark 1: *Ab-initio reconstruction of molecular structures via reverse Monte Carlo (MC) simulations has been explored in many recent studies[50,51]. Specifically, in reverse MC simulation methodology, starting from a random arrangement, the position of molecules is perturbed via MC moves with an objective to attain the target SAXS profiles. Although this method has been effective in attaining the target structures of protein and small colloids, it faces the primary challenge of generating many degenerate structures[51]. This challenge becomes significant when the size of self-assemblies becomes large, and the number of monomers involved increases. Ad-*

ditionally, the computational time taken for molecule-wise reverse MC simulations is very high, and in the case of large self-assemblies, computations become intractable [16,50,52]. Specifically, to avoid these challenges, our method combines SAXS information with thermodynamic knowledge from MC simulations to avoid degeneracy. Additionally, we coarse-grain our models and sample from a library of structures, which allows us to gain high computational efficiency over reverse MC simulation methodology and keeps our method computationally tractable.

3 System description and coarse-grained model development

In this section, the DBC system is explained in detail. Subsequently, the all-atom and coarse-grained representation of the monomers forming the DBC system is presented.

3.1 System description

DBCs are dynamic nanostructures formed by the interactions of ions, amphiphiles and solvent, i.e., DTA, OAPB and water molecules. A detailed description of the synthesis of OAPB can be found in the work of Liu et al[7]. Specifically, DBC system is prepared by mixing the zwitterionic amphiphile, OAPB, with DTA at a molar ratio of 3:1. Specifically, the suspension was homogenized via SJIA-2000W probe sonication (Ningbo Haishu Sklon Electronic Instrument Co., Ltd., Ningbo, China) for 10 minutes at 20kHz frequency. The suspension pH was adjusted by dropwise addition of 50 mM HCl and 50 mM NaOH. It was observed from previous experimental studies that in DBCs formed by OAPB and DTA ions, pH 6 is the rheologically important regime and at pH 9 the viscosity of these materials becomes significantly low.

3.2 Coarse-grained model

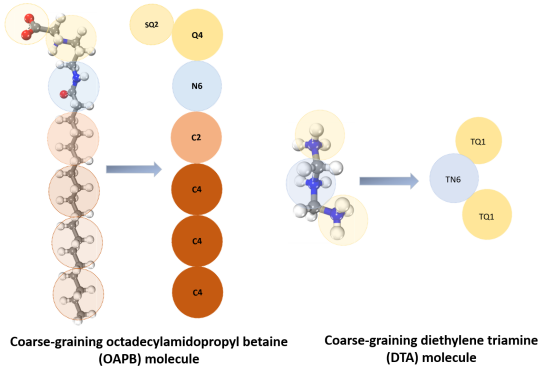

Fig. 2 Coarse-graining octadecylamidopropyl betaine (OAPB) and diethylene triamine (DTA) molecules.

The seeded nanostructures considered for MC simulations are modeled by the self-assembly of OAPB monomers and DTA ions. However, as DBCs can have dimensions close to a few hundreds of nanometers, a large number of monomers are required to be considered to model such large structures. Therefore, considering the atomistic description of these monomers makes the MC simulations computationally intractable. To reduce the number of interacting centers in the MC simulations, coarse-graining of DTA, OAPB, and water molecules is done using beads available in the Martini-3 force-field. To derive the coarse-grained model for the OAPB and DTA molecules, a map between the atomistic and coarse-grained beads is derived in a trial-and-error manner[39]. The initial guess of this map is primarily based on the structural knowledge of the molecules. Subsequently, this map is improved based on the mismatch between the results of coarse-grained and all-atom simulations. The final coarse-grained model derived for OAPB and DTA molecules is highlighted in Fig. 2.

It is important to observe that the energy profiles obtained for the number pressure temperature (NPT) coarse-grained and atomistic NPT sampling methodology are significantly different (Fig. 3a and Fig. 3b). In the NPT CGMC sampling process, the total potential energy of system reaches the equilibrium three orders of magnitude faster with the coarse-grained model than the all-atom model. Furthermore, in the coarse-grained model, the total potential energy of the NPT ensemble decreases in a logarithmic manner with the number of sweeps, while in the all-atom model, it decreases linearly. This highlights the fact that in the CGMC simulations, the computational efficiency would be significantly enhanced by utilizing the coarse-grained model.

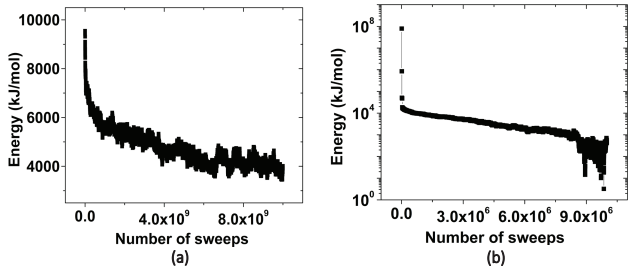

Fig. 3 Comparison of the total potential energy profiles, (1 sweep = 300 MC steps): (a) coarse-grained MC sampling, and (b) atomistic MC sampling methodology.

The comparison of bond-length distributions obtained from the coarse-grained and all-atom simulations for the covalent bonds in the amphiphilic tails (C4-C4) and the head group (Q4-N6) of the OAPB molecules are highlighted in Fig. 4a and Fig. 4b, respectively. The bond length distribution (TQ1-TN6) obtained from the atomistic and coarse-grained simulation of DTA molecules is highlighted in Fig. 4c. The density obtained from OAPB constant number pressure temperature (NPT) atomistic simulations is 978.0535 kg/m^3 while the density obtained from the corresponding coarse-grained simulations is 997.803 kg/m^3. The density of DTA is obtained as 866.458 kg/m^3 from atomistic simulations, while its counterpart from coarse-grained simulations is 868.032 kg/m^3.

4 Results and discussion

In this section, the implementation of the SAXS-guided unbiased CGMC simulation to sample the detailed three dimensional nanostructure of DBCs is highlighted. Then a detailed analysis providing insights into the pH tunability of DBCs is discussed. Finally, a few important insights into the structural features of DBCs are highlighted.

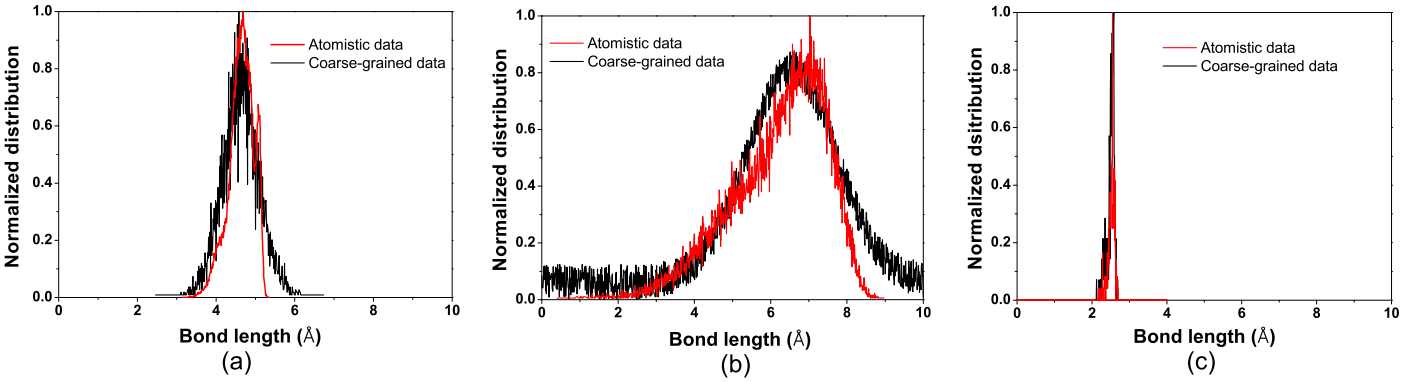

Fig. 4 Comparing atomistic and coarse-grained bond length distributions: (a) OAPB tail bond length, (b) OAPB head-group bond length, and (c) DTA bond length.

4.1 Structural identification via SAXS-guided unbiased CGMC

Owing to the inherent ambiguity of SAXS data analysis in predicting the three-dimensional nanostructures of self-assemblies, it is essential that another metric needs to be introduced that can aid us in reconstructing the unique three-dimensional nanostructure of DBCs. In this regard, we consider both SAXS discrepancy values and the total potential energy of DBCs obtained at equilibrium. This is shown by plotting the total potential energies of the nanostructures available from the SAXS-guided unbiased CGMC simulation scheme with respect to their SAXS discrepancy values in Fig. 5. It is observed that the sampling procedure begins with seeding nanostructures that have high total potential energy and high SAXS discrepancy values, as shown in the upper-right portion of the plot. However, as the sampling procedure progresses, the total potential energy and the SAXS discrepancy values of the sampled nanostructures decrease. This is evident by comparing the SAXS discrepancy values and the total potential energies at the 10^{th} and the 320^{th} iterations of the sampling process. We observe that by combining SAXS discrepancy values with CGMC simulation results, we can sample nanostructures that result in SAXS profiles closer to the target (i.e., one obtained from experiments) and are also thermodynamically favorable. Henceforth, the SAXS-guided unbiased CGMC sampling process terminates in the final iteration when we can no longer seed nanostructures that improve the SAXS discrepancy values or reduce the total potential energy of the system.

It is observed from Fig. 5, that the total number of seeded nanostructures eventually converges to only a few as the SAXS-guided unbiased CGMC sampling scheme proceeds. This is evident by comparing the number of nanostructures seeded at the 80^{th} and 320^{th} iterations. This is because, towards the end of sampling, many seeded nanostructures start having identical dimensions, resulting in convergence. We observe that at the end of the sampling procedure, we are left with four nanostructures (corresponding to the points highlighted in red in Fig. 5) that have identical SAXS discrepancy values but different energy values. This clearly indicates that based on the SAXS scattering profile only, it is impossible to identify the most probable nanostructure of DBCs as multiple geometrically discrete nanostructures have very similar SAXS profiles according to their discrepancy values[30].

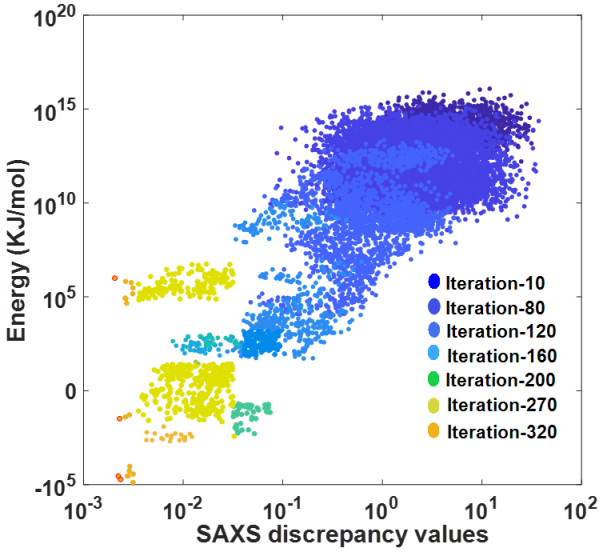

Fig. 5 SAXS discrepancy values, and total potential energy values at different iterations of the SAXS-guided unbiased CGMC sampling approach.

Table 1 Geometrical dimensions of the four nanostructures obtained from the SAXS-guided unbiased CGMC simulation.

Geometry	Cross section dimensions		
Bilayer cylinder	Inner layer	Diameter	
		119.5 nm	
	Outer layer	Diameter	
		191.3 nm	
Bilayer small ellipse	Inner layer	Minor axis	Major axis
		50.6 nm	68.7 nm
	Outer Layer	Minor axis	Major axis
		142.2 nm	157.5 nm
Bilayer larger ellipse	Inner layer	Minor axis	Major axis
		138.6 nm	156 nm
	Outer layer	Minor axis	Major axis
		212 nm	226.5 nm
Rod like	Diameter		
	217.4 nm		

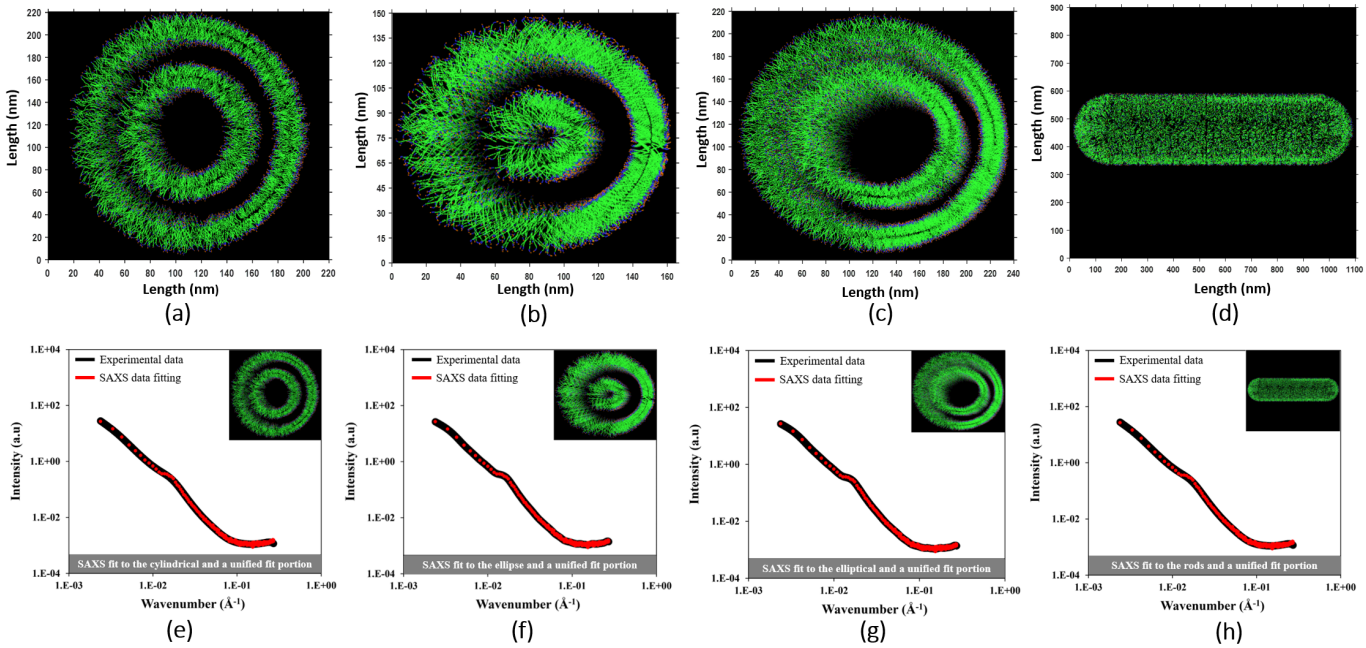

Fig. 6 Four nanostructures obtained from the SAXS-guided unbiased CGMC sampling approach which have degenerate SAXS discrepancy values: (a) bilayer cylindrical assembly, (b) bilayer small elliptical assembly, (c) bilayer large elliptical assembly, and (d) rod like cylindrical assembly. Final SAXS fitting to the four different nanostructures: (e) bilayer cylindrical nanostructure, (f) bilayer smaller ellipse nanostructure, (g) bilayer larger ellipse structure, and (h) cylindrical rod-like nanostructures.

To further highlight the ambiguity resulting from analyzing SAXS scattering profiles alone, we present the four nanostructures having the least SAXS discrepancy values along with their SAXS scattering profiles in Fig. 6. These results clearly show that all of the nanostructures have identical SAXS profiles despite having significantly different geometries (Fig. 6 and Table 1). Hence another metric must be defined that can aid us to eliminate this inherent ambiguity.

By comparing the energy profiles of the four nanostructures in Fig. 7, it is clear that these nanostructures have very different energy values. Furthermore, on observing the four nanostructures obtained from the CGMC simulation at equilibrium, it is clearly understood that one of these nanostructures completely dismantles (Fig. 8b), thus highlighting its low probability of being the nanostructure of DBCs. This idea is also supported by the results from energy profiles (Fig. 7). Specifically, the nanostructure with the least alignment at equilibrium has the highest energy among all four, hence the lowest probability of being the nanostructure of DBCs. Likewise, the nanostructure which has the best alignment at equilibrium (Fig. 8c) has the least energy and hence is concluded as the most probable nanostructure of DBCs. Therefore, we show that by simultaneously considering the two metrics, structural information from SAXS and thermodynamic insights from MC simulations, we could clearly identify the unique three-dimensional nanostructure of DBCs and resolve the ambiguity associated with SAXS-only data analysis. Additionally, from the SAXS profiles obtained by the CGMC simulations (i.e., Fig. 8e-h), we observe that the SAXS profiles for bilayer larger ellipse and cylindrical rod-like structures have excellent agreement with the experimental data. On the other hand, the SAXS profiles for the bilayer cylindrical and the bilayer smaller elliptical structures are different from the experimental data. The result clearly shows that the most probable structure of DBCs sampled via the SAXS-guided CGMC simulation strategy (i.e., the bilayer larger elliptical structure) stays stable at equilibrium and the SAXS profile obtained from it matches with the target SAXS profile that are obtained from the experiments.

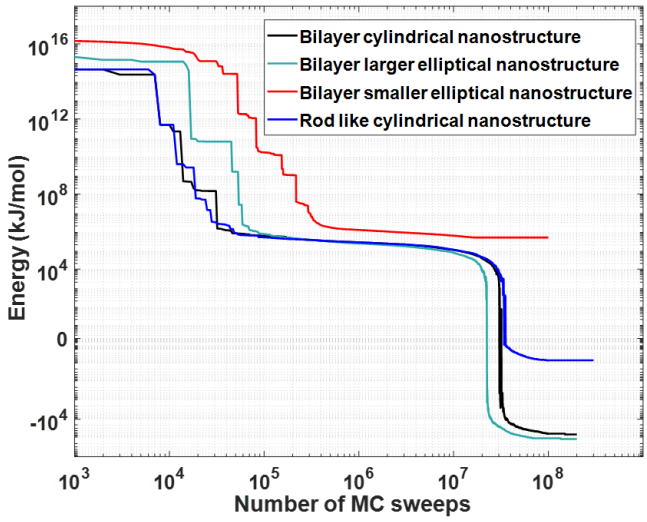

Fig. 7 The total potential energy profile of the four nanostructures obtained from the SAXS-guided unbiased CGMC simulation.

Remark 2: *It is to be noted that the interaction potential of the molecules is not biased by any means so the accuracy of the thermodynamic calculations is high. Since the thermodynamic results*

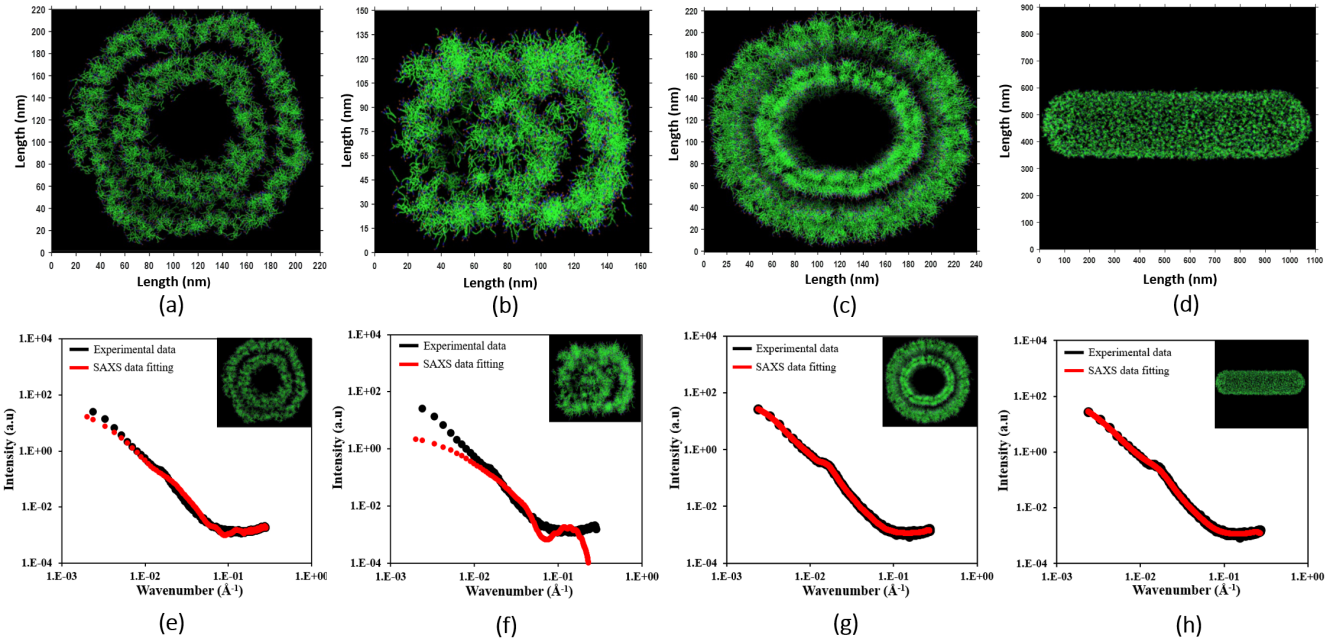

Fig. 8 The four nanostructures obtained at equilibrium from the SAXS-guided CGMC simulation: (a) bilayer cylindrical assembly, (b) bilayer small elliptical assembly, (c) bilayer large elliptical assembly, and (d) rod like cylindrical assembly. Comparison of the corresponding SAXS profiles of the equilibrium structures with experimental results: (e) bilayer cylindrical nanostructure, (f) bilayer smaller ellipse nanostructure, (g) bilayer larger ellipse structure, and (h) cylindrical rod-like nanostructures.

are accurate, the choice of the total potential energy of the system as a metric to distinguish nanostructures having degenerate SAXS profiles is also justified.

It is to be noted that while performing CGMC simulations, the aforementioned nanostructures are solvated with water molecules, when the DTA to amphiphile ratio is 1:3 (i.e., the value considered in experimental formulation [7]). All the nanostructures have DTA ions which are initially placed at a distance of 7 nm from the OAPB surface. The images of most probable nanostructure of DBCs with DTA ions before and after equilibration are shown in Fig. 9.

Remark 3: *In preparing for the initial nanostructures for the CGMC simulations, the distance of the DTA ions is kept to be 7 nm from the OAPB surface. However, for the stable bilayer ellipse structure at equilibrium, the mean distance among the DTA ions is 6.1 nm from the surface of the inner ellipse and 10 nm from the surface of the outer ellipse.*

4.2 Experimental verification

In order to validate the findings, SEM images (Fig. 10) of the DBCs formed by OAPB and DTA ions are obtained. Specifically, these images highlight the elongated entangled structures that are formed by the network and aggregation of the micelles. Due to the frozen drying process which forms the large aggregates, the entanglement and elongated structure of micelles could look similar to the elongated layered elliptical nanostructures found from SAXS and CGMC simulations. Furthermore, in the SEM image with higher magnification, the single elongated layered elliptical nanostructures of the micelle could be clearly observed on the large aggregated surfaces, which validates the single shape obtained from the SAXS and CGMC simulations. Meanwhile, the diameter of the single elliptical nanostructures in the large aggregates was determined at 200 nm, which is very close to the major and minor axis values of the outer ellipse of bilayer larger structure obtained from the SAXS-guided unbiased CGMC simulation.

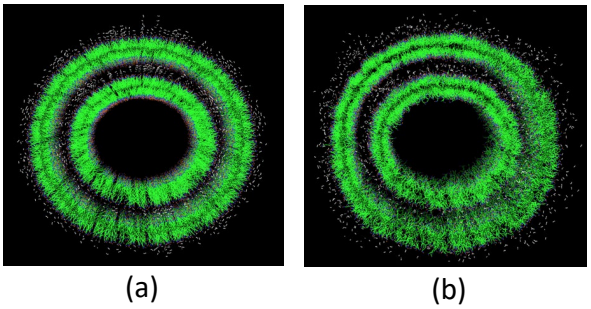

Fig. 9 The relative position of the DTA ions: (a) initial state of the DTA and OAPB molecules, and (b) final state the DTA and OAPB molecules after the SAXS-guided unbiased CGMC simulations.

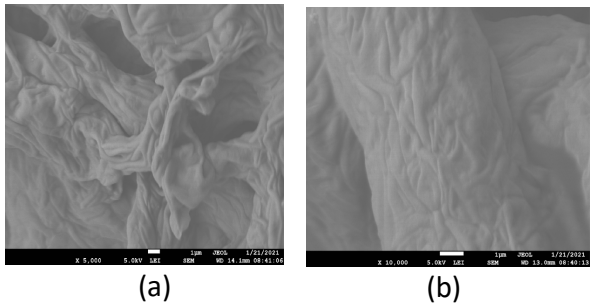

Fig. 10 The SEM images of the solution formed by OAPB and DTA ions: (a) formation of entangled structure, and (b) aggregated entangled elongated structures.

As mentioned previously and is evident from the results in this section, with imaging techniques like SEM, samples are dehydrated, and hence aggregation of the nanostructures is clearly observed. Therefore, we cannot observe the exact layered nanostructures of the DBCs with SEM images here. This reiterates the advantage of using the SAXS-guided CGMC simulations over conventional experimental characterization methods. Specifically, SAXS-guided CGMC simulations aid us in accurately obtaining the three-dimensional nanostructures of DBCs by using the SAXS diffraction pattern from the dispersed phase of DBCs alongside CGMC simulations.

Remark 4: *In the case of DBCs, polydispersity would exist in the cross-section (i.e., the major axis of the ellipse) and length directions. However, the polydispersity in the length direction does not significantly affect the SAXS intensity profiles. Since the length of DBCs extends to a few micrometers, X-ray scattering from these length-scales takes place at very low angles that are not captured in the SAXS experiments[53,54]. To analyze the case of polydispersity in the major axis of the tubular elliptical structures, we evaluate an approximate size distribution of the major axis of the elliptical tubular structure from the SEM images. This evaluated distribution is highlighted in Fig. 11. The PDI value obtained from this distribution is 4.15%. It is to be noted that for PDI values less than 10%, multiple studies have proved that a molecular-level reconstruction of nanostructures is possible from SAXS data, and monodisperse form factors can conviniently be considered in the SAXS data analysis[55,56]. Therefore, following the validity of this widely accepted assumption the effect of polydispersity has not been considered in the proposed framework.*

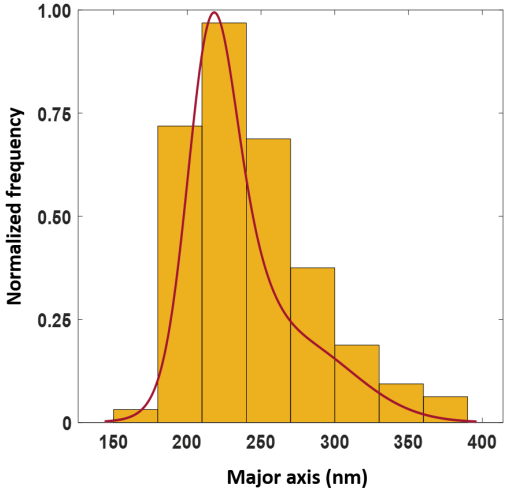

Fig. 11 Size distribution of the major axis of the tubular nanostructures.

4.3 Analyzing the significance of ions in providing pH tunability

Experimental studies highlight that at room temperature (i.e., 298 K) the viscosity of the DBCs decreases as the pH of the solution changes from 6 to 9. We attribute this property change to the varying degree of ionization for the DTA molecules. Specifically, at pH of 6 or below, DTA molecules carry two or more charges. However, beyond pH of 9.2, DTA molecules have a single charge. This is understood from the pKa values of the DTA molecule which are highlighted as follows:

$$\mathrm{NH_2C_2H_4NHC_2H_4NH_2} \xrightarrow[\mathrm{pKa}=10.07]{\mathrm{H^+}} \mathrm{NH_3^+C_2H_4NHC_2H_4NH_2}$$

$$\mathrm{NH_3^+C_2H_4NHC_2H_4NH_2} \xrightarrow[\mathrm{pKa}=9.21]{\mathrm{H^+}} \mathrm{NH_3^+C_2H_4NHC_2H_4NH_3^+}$$

$$\mathrm{NH_3^+C_2H_4NHC_2H_4NH_2} \xrightarrow[\mathrm{pKa}=4.42]{\mathrm{H^+}} \mathrm{NH_3^+C_2H_4NH_2^+C_2H_4NH_3^+}$$

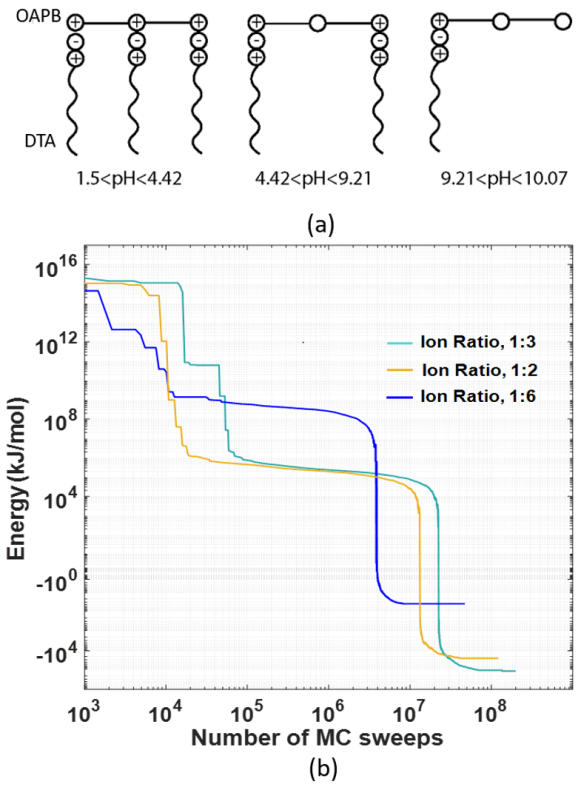

Fig. 12 Insights into pH tunability of DBCs: (a) changing charge to amphiphile ratio with varying pH, and (b) energy profiles obtained from the SAXS-guided unbiased CGMC sampling of DBCs with varying ion to amphiphile ratios.

Since the varying degree of ionization of the DTA molecules changes the ion to amphiphile ratio in the solution, we hypothesize that this change will have a significant impact on the structure of DBCs which should finally affect their viscoelasticity. To test this hypothesis, we performed CGMC simulations with the identified structure of DBC by varying the DTA molecules to amphiphile ratio as 1:2, 1:3, and 1:6. It is to be noted that these ratios correspond to the charge to amphiphile ratios of 1:1, 2:3, and 1:3, respectively, which correspond to solution conditions at pH values of 4, 6, and 9.2, respectively, as is highlighted in Fig. 12a. The energy profile obtained from CGMC sampling of DBCs under

the varying solution conditions is highlighted in Fig. 12b. These results show that the total potential energy of DBCs increases significantly at low values of DTA to amphiphile ratio (i.e., at 1:6). This is because the interaction between the DTA molecules and amphiphilic head-groups (SQ2-TQ1) has a negative contribution to the total potential energy, and this contribution decreases on reducing the ion to amphiphile ratio. Furthermore, when increasing the value of DTA molecule to amphiphile ratio from 1:3 to 1:2, the total potential energy of DBCs is found to increase. This is because of the positive contribution to the total potential energy by the interactions among the charged centers of DTA molecules. Specifically, at a very high DTA concentrations, the repulsion energy between their charged centers is high, leading to increased total potential energy. The simulation snapshots for three different solution conditions, i.e., DTA to amphiphile ratio of 1:2, 1:3, and 1:6, are highlighted in Fig. 13. These results show that when the DTA to amphiphile ratio decreases from 1:3 to 1:6, the nanostructure of DBCs completely disassembles, which explains why DBCs loose their viscoelasticity at a high pH. However, at a low pH the nanostructure of DBCs does not change significantly, highlighting why DBCs can have good viscoelasticity even at low pH values close to 4.

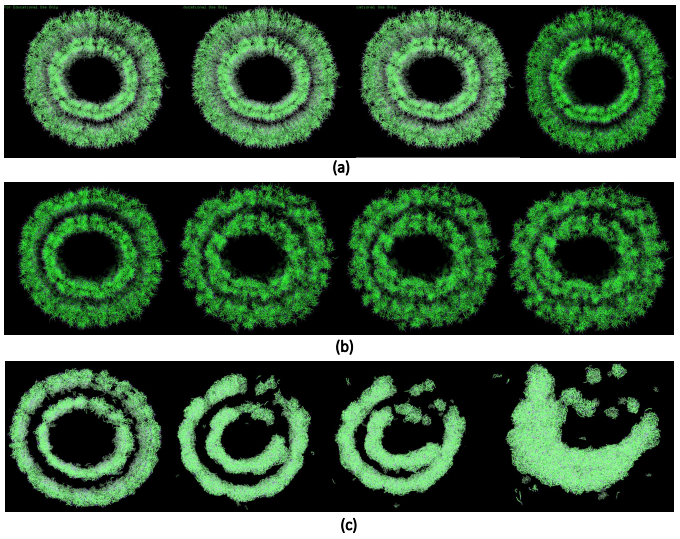

Fig. 13 The nanostructure of DBCs at different pH values: (a) pH 4, (b) pH 6, and (c) pH 9.2.

From the aforementioned results, it is noted that stronger interaction between the ions and amphiphiles drives the total potential energy of DBCs to lower values, which highlights that the presence of DTA molecules is crucial to the stability of DBCs. The pH tunability has made the application of DBCs to the oil and gas industry very prominent[57]; in particular, DBCs can be used to replace the conventional hydraulic fracturing approach using slick water to ones utilizing complex fluids like DBCs[58–60]. Furthermore, the insights we obtain in this work by performing a deeper analysis of the structure and stability of DBCs can allow us to extend their application across other industries by developing accurate structure-property relationships in future studies[61]. In future studies, an effective design of DBC based complex fluids can be considered by implementing the CGMC simulations developed in this work and by following the molecular design heuristics proposed in recent literature studies[34–36]. Additionally, an effective design of DBC based complex fluids can be considered by implementing the CGMC simulations developed in this work and by following the molecular design heuristics proposed in recent literature studies[34–36].

Remark 5: *To highlight the thermal stability of DBC microstructures, a plot of the SAXS discrepancy value of the structures obtained from CGMC simulations with increasing temperatures is shown in Fig. 14. It is apparent from Fig. 14 that the SAXS discrepancy values drastically change with increasing temperatures, and we observe that at a high temperature of 100°C, the DBCs completely disintegrate. We also note that at 50°C, the nanostructures are stable. This explains the higher thermal stability of DBCs than conventional WLMs, which degrade and lose their viscoelastic properties at temperatures of 50-60 °C*[62].

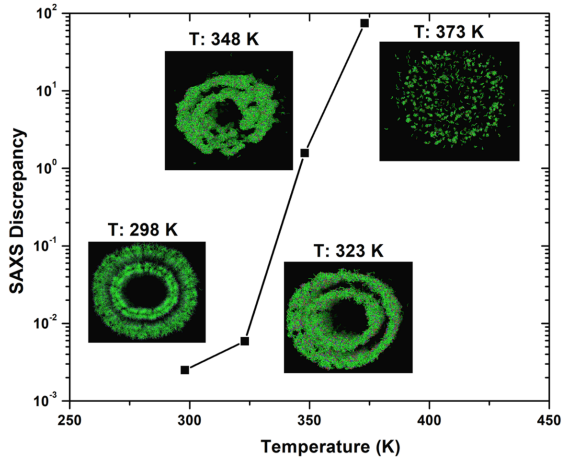

Fig. 14 Demonstration of the varying structural stability of DBCs with temperature.

5 Conclusion

SAXS-guided unbiased CGMC simulations were performed to study the detailed three dimensional nanostructure of self-assemblies called DBCs. In the SAXS-guided unbiased CGMC simulation, first, nanostructures are derived from the existing literature. Subsequently, multiple nanostructures are seeded from them by varying their characteristic dimensions. Then CGMC simulations are performed on these seed nanostructures to obtain a set of nanostructures that have the least energy and SAXS discrepancy values. Henceforth, in every iteration of the SAXS-guided unbiased CGMC simulation, the SAXS discrepancy values of the seeded nonstructures are observed to decrease, implying that after every iteration the sampled nanostructures result in SAXS profiles closer to the target. The procedure continues until the improvement in the SAXS discrepancy values and energy becomes insignificant. The results of the aforementioned procedure show that CGMC simulations can be a complementary method that can aid us to fully interpret the limited structural information present in the SAXS data. The hybrid information obtained from SAXS and CGMC simulations helps us clearly identify the nanostructure and dimensions of DBCs. Specifically, the bilayer ellipse

nanostructure is determined as the most probable nanostructure of DBCs. The dimensions of the obtained nanostructures were validated with experimental results from SEM images. Subsequently, using the molecular description of the derived nanostructures, the effect of pH on these nanostructures was highlighted. The obtained results could explain the observations reported in the previous literature.

6 Acknowledgment

The authors gratefully acknowledge financial support from the Department of Energy (DE-FE0031778, DE-EE0007888-10-8), the Texas A&M Energy Institute, the Artie McFerrin Department of Chemical Engineering, and the Texas A&M High Performance Research Computing facility.

Notes and references

1 D. Wu, W. Zou, H. Quan, B. Wei, H. Yin and Y. Feng, *Journal of Molecular Liquids*, 2021, **325**, 114656.
2 G. Maitland, *Current Opinion in Colloid & Interface Science*, 2000, **5**, 301–311.
3 D. S. Yakovlev and E. S. Boek, *Langmuir*, 2007, **23**, 6588–6597.
4 Q. Chen, W. Liu, H. Liu, X. Huang, Y. Shang and H. Liu, *Langmuir*, 2020, **36**, 9499–9509.
5 S. Pahari, J. Moon, M. Akbulut, S. Hwang and J. S.-I. Kwon, *Chemical Engineering Research and Design*, 2021, **174**, 30–41.
6 B. Bhat, S. Liu, Y.-T. Lin, M. L. Sentmanat, J. Kwon and M. Akbulut, *PloS One*, 2021, **16**, e0260786.
7 S. Liu, Y.-T. Lin, B. Bhat, K.-Y. Kuan, J. S.-I. Kwon and M. Akbulut, *RSC Advances*, 2021, **11**, 22517–22529.
8 S. Zaefferer, *Crystal Research and Technology*, 2011, **46**, 607–628.
9 A. P. Gelissen, A. Oppermann, T. Caumanns, P. Hebbeker, S. K. Turnhoff, R. Tiwari, S. Eisold, U. Simon, Y. Lu, J. Mayer *et al.*, *Nano Letters*, 2016, **16**, 7295–7301.
10 S. Helvig, I. D. Azmi, S. M. Moghimi and A. Yaghmur, *Aims Biophysics*, 2015, **2**, 116–130.
11 R. M. Glaeser, *Annual Review of Biochemistry*, 2021, **90**, 451–474.
12 F. Scheffold, *Nature Communications*, 2020, **11**, 1–13.
13 D. Svergun, C. Barberato and M. H. Koch, *Journal of Applied Crystallography*, 1995, **28**, 768–773.
14 B. Angelov, A. Angelova, M. Drechsler, V. M. Garamus, R. Mutafchieva and S. Lesieur, *Soft Matter*, 2015, **11**, 3686–3692.
15 P. V. Konarev, M. V. Petoukhov, V. V. Volkov and D. I. Svergun, *Journal of Applied Crystallography*, 2006, **39**, 277–286.
16 M. Li, W. Wang and P. Yin, *Chemistry*, 2018, **24**, 6639–6644.
17 L. Feigin, D. I. Svergun *et al.*, *Structure analysis by small-angle X-ray and neutron scattering*, Springer, 1987, vol. 1.
18 F. Herranz-Trillo, M. Groenning, A. Van Maarschalkerweerd, R. Tauler, B. Vestergaard and P. Bernadó, *Structure*, 2017, **25**, 5–15.
19 M. V. Petoukhov and D. I. Svergun, *Acta Crystallographica Section D: Biological Crystallography*, 2015, **71**, 1051–1058.
20 S. Yang, *Advanced Materials*, 2014, **26**, 7902–7910.
21 T. N. Cordeiro, F. Herranz-Trillo, A. Urbanek, A. Estaña, J. Cortés, N. Sibille and P. Bernadó, *Current Opinion in Structural Biology*, 2017, **42**, 15–23.
22 P. V. Konarev and D. I. Svergun, *IUCrJ*, 2015, **2**, 352–360.
23 S. Pahari, B. Bhadriraju, M. Akbulut and J. S.-I. Kwon, *Journal of Colloid and Interface Science*, 2021, **600**, 550–560.
24 W. Zou, X. Tang, M. Weaver, P. Koenig and R. G. Larson, *Journal of Rheology*, 2015, **59**, 903–934.
25 D. Kimanius, I. Pettersson, G. Schluckebier, E. Lindahl and M. Andersson, *Journal of Chemical Theory and Computation*, 2015, **11**, 3491–3498.
26 J. S. Hub, *Current Opinion in Structural Biology*, 2018, **49**, 18–26.
27 M. Chan-Yao-Chong, D. Durand and T. Ha-Duong, *Journal of Chemical Information and Modeling*, 2019, **59**, 1743–1758.
28 M. R. Hermann and J. S. Hub, *Journal of Chemical Theory and Computation*, 2019, **15**, 5103–5115.
29 S. A. Hollingsworth and R. O. Dror, *Neuron*, 2018, **99**, 1129–1143.
30 C. Zhao and D. Shukla, *Scientific Reports*, 2018, **8**, 1–13.
31 B. A. Berg, *Phys.Stat. Mech*, 2005, **7**, 1–52.
32 M. Quesada-Pérez and A. Martín-Molina, *Soft Matter*, 2013, **9**, 7086–7094.
33 T. J. Weyer and A. R. Denton, *Soft Matter*, 2018, **14**, 4530–4540.
34 D. Valencia-Marquez, A. Flores-Tlacuahuac, A. J. García-Cuéllar and L. Ricardez-Sandoval, *Computers & Chemical Engineering*, 2022, **156**, 107523.
35 U. Abdulfatai, A. Uzairu, G. A. Shallangwa and S. Uba, *Journal of Bio-and Tribo-Corrosion*, 2020, **6**, 1–9.
36 D. Chaffart, S. Shi, C. Ma, C. Lv and L. A. Ricardez-Sandoval, *The Journal of Physical Chemistry B*, 2022, **126**, 2040–2059.
37 J. K. Shah, E. Marin-Rimoldi, R. G. Mullen, B. P. Keene, S. Khan, A. S. Paluch, N. Rai, L. L. Romanielo, T. W. Rosch, B. Yoo *et al.*, *Cassandra: An open source Monte Carlo package for molecular simulation*, 2017.
38 S. J. Marrink, H. J. Risselada, S. Yefimov, D. P. Tieleman and A. H. De Vries, *The Journal of Physical Chemistry B*, 2007, **111**, 7812–7824.
39 P. C. Souza, R. Alessandri, J. Barnoud, S. Thallmair, I. Faustino, F. Grünewald, I. Patmanidis, H. Abdizadeh, B. M. Bruininks, T. A. Wassenaar *et al.*, *Nature Methods*, 2021, **18**, 382–388.
40 Q. Meng, Y. Kou, X. Ma, Y. Liang, L. Guo, C. Ni and K. Liu, *Langmuir*, 2012, **28**, 5017–5022.
41 G. Zaldivar, S. Vemulapalli, V. Udumula, M. Conda-Sheridan and M. Tagliazucchi, *The Journal of Physical Chemistry C*, 2019, **123**, 17606–17615.
42 H. Cui, M. J. Webber and S. I. Stupp, *Peptide Science: Original Research on Biomolecules*, 2010, **94**, 1–18.
43 R. K. Kankala, S.-B. Wang and A.-Z. Chen, *Iscience*, 2020, **23**, 101687.
44 S. H. Seo, J. Y. Chang and G. N. Tew, *Angewandte Chemie*

International Edition, 2006, **45**, 7526–7530.

45 D. Liu, Y. Li, F. Liu, W. Zhou, A. Sun, X. Liu, F. Chen, B. B. Xu and J. Wei, *Polymers*, 2020, **12**, 265.

46 S. Izvekov, A. Violi and G. A. Voth, *The Journal of Physical Chemistry B*, 2005, **109**, 17019–17024.

47 J. J. Panda and V. S. Chauhan, *Polymer Chemistry*, 2014, **5**, 4418–4436.

48 J. Prates Ramalho, P. Gkeka and L. Sarkisov, *Langmuir*, 2011, **27**, 3723–3730.

49 M. S. Nikolic, C. Olsson, A. Salcher, A. Kornowski, A. Rank, R. Schubert, A. Frömsdorf, H. Weller and S. Förster, *Angewandte Chemie*, 2009, **121**, 2790–2792.

50 S. Yang, M. Parisien, F. Major and B. Roux, *The Journal of Physical Chemistry B*, 2010, **114**, 10039–10048.

51 A. T. Tuukkanen, G. J. Kleywegt and D. I. Svergun, *IUCrJ*, 2016, **3**, 440–447.

52 D. Franke, M. Petoukhov, P. Konarev, A. Panjkovich, A. Tuukkanen, H. Mertens, A. Kikhney, N. Hajizadeh, J. Franklin, C. Jeffries *et al.*, *Journal of applied crystallography*, 2017, **50**, 1212–1225.

53 S. Pikus, J. Jamroz and E. Kobylas, *Żywność-Nauka-Technologia-Jakość (Suplement)*, 2000, **2**, 160–168.

54 D. Pontoni, T. Narayanan and A. R. Rennie, *Journal of applied crystallography*, 2002, **35**, 207–211.

55 E. Shtykova, *Nanotechnologies in Russia*, 2015, **10**, 408–419.

56 S. Sakurai, *Chapter*, 2017, **5**, 107–134.

57 S. Pahari, P. Bhandakkar, M. Akbulut and J. S.-I. Kwon, *Energy*, 2021, **216**, 119231.

58 P. Siddhamshetty, K. Wu and J. S.-I. Kwon, *Industrial & Engineering Chemistry Research*, 2019, **58**, 3159–3169.

59 P. Siddhamshetty, S. Yang and J. S.-I. Kwon, *Computers & Chemical Engineering*, 2018, **114**, 306–317.

60 A. Narasingam, P. Siddhamshetty and J. Sang-Il Kwon, *AIChE Journal*, 2017, **63**, 3818–3831.

61 S. Pahari, J. Moon, M. Akbulut, S. Hwang and J. S.-I. Kwon, *Industrial & Engineering Chemistry Research*, 2021, **60**, 15669–15678.

62 E. J. Nodoushan, Y. J. Lee, H.-J. Na, B.-H. You, M.-Y. Lee and N. Kim, *Journal of Industrial and Engineering Chemistry*, 2021, **98**, 458–464.